Front. Earth Sci. 2021, 15(2): 237–255
https://doi.org/10.1007/s11707-020-0845-x

RESEARCH ARTICLE

Pore size distribution of high volatile bituminous coal of the southern Junggar Basin: a full-scale characterization applying multiple methods

Wanchun ZHAO[1], Xin LI (✉)[1,2], Tingting WANG[1,3], Xuehai FU[2,4]

1 Key Laboratory of Continental Shale Accumulation and Development (Ministry of Education), Northeast Petroleum University, Daqing 163000, China
2 School of Geology and Mining Engineering, Xinjiang University, Urumqi 830047, China
3 School of Electrical Engineering and Information, Northeast Petroleum University, Daqing 163000, China
4 School of Resources & Earth Science, China University of Mining & Technology, Xuzhou 221008, China

Abstract Studying on the pore size distribution of coal is vital for determining reasonable coalbed methane development strategies. The coalbed methane project is in progress in the southern Junggar Basin of northwestern China, where high volatile bituminous coal is reserved. In this study, with the purpose of accurately characterizing the full-scale pore size distribution of the high volatile bituminous coal of the southern Junggar Basin, two grouped coal samples were applied for mercury intrusion porosimetry, low-temperature nitrogen adsorption, low-field nuclear magnetic resonance, rate-controlled mercury penetration, scanning electron microscopy, and nano-CT measurements. A comprehensive pore size distribution was proposed by combining the corrected mercury intrusion porosimetry data and low-temperature nitrogen adsorption data. The relationship between transverse relaxation time (T_2, ms) and the pore diameter was determined by comparing the T_2 spectrum with the comprehensive pore size distribution. The macro-pore and throat size distributions derived from nano-CT and rate-controlled mercury penetration were distinguishingly analyzed. The results showed that: 1) comprehensive pore size distribution analysis can be regarded as an accurate method to characterize the pore size distribution of high volatile bituminous coal; 2) for the high volatile bituminous coal of the southern Junggar Basin, the meso-pore volume was the greatest, followed by the transition pore volume or macro-pore volume, and the micro-pore volume was the lowest; 3) the relationship between T_2 and the pore diameter varied for different samples, even for samples with close maturities; 4) the throat size distribution derived from nano-CT was close to that derived from rate-controlled mercury penetration, while the macro-pore size distributions derived from those two methods were very different. This work can deepen the knowledge of the pore size distribution characterization techniques of coal and provide new insight for accurate pore size distribution characterization of high volatile bituminous coal.

Keywords pore size distribution, coalbed methane, high volatile bituminous coal, low field nuclear magnetic resonance, the southern Junggar Basin

Received June 10, 2020; accepted October 10, 2020

E-mail: lixinwaxj@xju.edu.cn

1 Introduction

The pores and fractures of coal provide spaces for coalbed methane (CBM) desorption and diffusion as well as seepage (Yao and Liu, 2012; Okolo et al., 2015; Zhou et al., 2017a) during the process of CBM production. The pore size distribution (PSD) of coal can effectively demonstrate the development degrees of pores with different scales (Zhou et al., 2018a). Based on PSD identification, CBM geologists cannot only judge the gas bearing capacity and permeability of coal reservoir, but also evaluate the reservoir conditions and predict the CBM development potential (Karacan and Okandan, 2000; Fu et al., 2017; Song et al., 2017). According to the characteristics of methane adsorption and migration in pores with different sizes, Ходот (1966) proposed a scheme for pore classification, which has been widely applied in study of CBM reservoirs (Kang et al., 2018; Zhang et al., 2018), namely micro-pores (<0.01 μm), transitional pores (0.01–0.1 μm), meso-pores (0.1–1 μm), and macro-pores (>1 μm).

The methods and technologies characterizing the PSD of coal have been continually improved. Outcrop observations (Cooper et al., 2007) and optical microscope observations of coal (Cai et al., 2011; Zhao et al., 2017; Zhou et al., 2018b; Wang et al., 2018), providing first-hand geological information for the evaluation of CBM reservoirs, were initially applied to characterize PSD of coal. Subsequently, multiple methods such as mercury intrusion porosimetry (MIP; Yao et al., 2009; Zhou et al., 2017b), low temperature nitrogen adsorption (LTNA; Song et al., 2017), scanning electron microscopy (SEM; Liu and Nie, 2016), and transmission electron microscopy (Zhao and Ren, 1995), developed rapidly during the second half of last century, making high-resolution characterizations of pore morphology and full-scale characterization of PSD realistic. In recent years, new technologies including small angle X-ray scattering (Bale and Schmidt, 1984; Pan et al., 2016; Sang et al., 2018; Liu et al., 2019), low field nuclear magnetic resonance (LF-NMR; Yao et al., 2010a, 2010b), micro-computed tomography (Micro-CT; Bai et al., 2013; Li et al., 2017b; Ni et al., 2017; Shi et al., 2018), rate-controlled mercury penetration (CMP; Yao and Liu, 2012), and focused ion beam scanning electron microscopy (FIB-SEM; Gomord et al., 2017), have been used to characterize the PSD of coal, which has further enhanced the characterization resolution and accuracy and effectively improved the research depth of coal microscopic desorption and gas and water seepage mechanisms. Although technologies with different precisions have been widely applied in the joint characterization of the PSD of coal, two deficiencies still exist: 1) previous comparative studies on the PSD are mainly limited to using MIP and another method (LTNA, LF-NMR, or micro-CT). MIP data may not be correct considering that the coal matrix is compressed under high pressure, leading to the occurring of errors during the process of the transfer from T_2 value of LF-NMR data to pore diameter; 2) the macro-pore and throat size distribution characterization methods were scarcely analyzed and distinguished.

To address the above two issues and with the purpose of deepening CBM exploration theories of the southern Junggar Basin (SJR), where high-volatile bituminous coal (HVBC) was deposited, the pore characteristics of HVBC in the SJR were characterized using multiple methods, including MIP, LTNA, LF-NMR, CMP, SEM, and nano-CT. The comprehensive pore size distribution (CPSD) characterization combining LTNA data and corrected MIP data was first reported in this work. The relationship between T_2 and the pore diameter was determined by comparing the CPSD and LF-NMR data. The macro-pore and throat size distribution characterizations using CMP and Nano-CT were distinguished and analyzed. The results of this work can deepen the knowledge on the PSD of coal.

2 Geological background

HVBC are accumulated in the Mesozoic coal measures in the SJR (Fig. 1(a)), north-western China, where the samples of this study were collected. The SJR is characterized by a multi-depositional and multi-type structural system including reverse faults and anticlines as well as synclines (Guan et al., 2012), covering an area of 6035 km^2 (Zhou et al., 2016) (Fig. 1(a)). The Lower Jurassic Badaowan Formation (J_{1b}) and the Middle Jurassic Xishanyao Formation (J_{2x}) are main coal-bearing strata (Fig. 1(b)) (Li et al., 2019). The coal samples of this

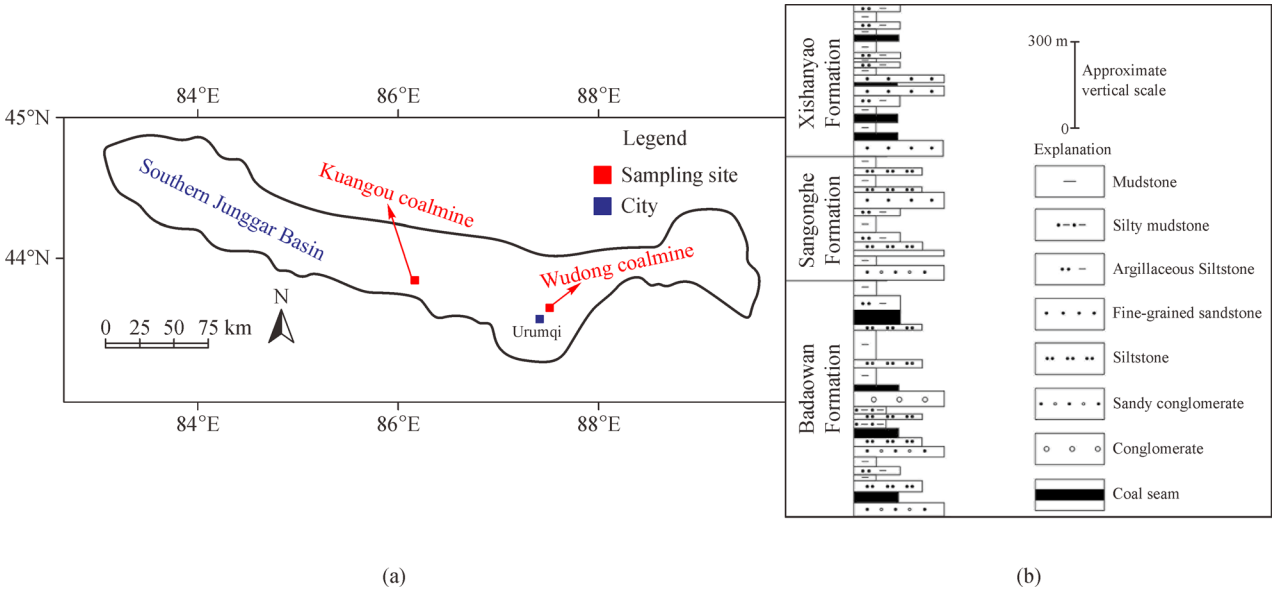

Fig. 1 (a) Sampling sites in the SJR (after Zhou et al. (2016)); (b) Generalized coal-bearing stratigraphic column for the SJR (after Tian and Yang (2011)).

study were collected from the J_{1b} consisting of glutenite, siltstone, silty mudstone, gray mudstones and interbedded coal seams (Mao and Xu, 1999). The CBM resources are 3.54×10^{12} m^3 in the SJR (Zhou et al., 2016). Recently a CBM development block named Baiyanghe was established as the first demonstration base of CBM development in the SJR (Fu et al., 2016), with annual gas production of 30 million m^3 (Li et al., 2018). This progress in CBM development demonstrates good prospects for CBM development in the SJR.

3 Methods

Figure 2 displays the workflow of this study. The CPSD of HVBC were studied by combining the corrected MIP data and LTNA data. The relationship between T_2 and the pore diameter was determined by comparing T_2 spectrum with the CPSD, and then, the PSD derived from LF-NMR (NMR-PSD) was determined. Comparative analyses of the macro-pore and throat size distributions derived from nano-CT and CMP were conducted. In addition, SEM was applied to verify the accuracies of the CPSD and NMR-PSD. The pore size classification of Ходот (1966) stating that the diameters of the micro-pores, transition pores, meso-pores and macro-pores are < 10 nm, 10–100 nm, 100–1000 nm, and > 1000 nm, respectively, was applied in this research. The pictures of all the experimental facilities can be seen in Fig. 3, and the details of the procedures of these experiments are introduced as follows.

3.1 Sample collection and treatment

Coal blocks (approximately 30 cm × 30 cm × 30 cm) were sampled from the Wudong coalmine (WD) and Kuangou coalmine (KG) located in the SJR (Fig. 1). The basic measurements of the maximum vitrinite reflectance, proximate analysis, and coal composition were conducted using the collected samples, according to the standards of ISO 7404-5-2009, ISO 17246-2010 and ISO 7404-3-2009, respectively (Table 1). The samples from the WD and KG are HVBC, according to the American Society of Testing Materials Standard ASTM D388-2015.

The geometric specifications of the samples used in different experiments are different due to the differences in the experimental principles. Taking MIP, LF-NMR, CMP, and LTNA samples for instance, the experimental principles of the former three can be summarized as volume detection by injecting fluid, hence, cylindrical samples are required for convenient and smooth injection; however, the principle of LTNA is to detect the adsorbed liquid nitrogen volume, hence, powder samples are required to ensure the accuracy. In this work, the samples were categorized into six types from the same block coal, abbreviated to S-I, S-II, S-III, S-IV, S-V, and S-VI, which were used for the MIP, LTNA, LF-NMR, CMP, SEM, and Nano-CT experiments, respectively. The details on these samples are introduced as follows.

S-I were cylindrical coal samples used for the MIP tests, with dimensions of 10 mm in height and 25 mm in diameter. S-II were 60–80 meshed powder coal samples applied for the LTNA tests. S-III, used for the LF-NMR measurements, were cylindrical coal cores 25 mm in diameter and 30 mm in length. S-IV were cylindrical coal samples used for the CMP tests, with dimensions of 10 mm in height and 25 mm in diameter. S-V were 10 mm × 10 mm × 3 mm in dimension and used for the SEM observations. S-VI was a needle sample, which was used for the nano-CT test, with dimension of 1 mm in length and 1 mm in diameter. It should be noted that S-I, S-III, and S-IV were obtained by cutting the same long cylindrical sample, which was drilled along the direction parallel to the bedding plane from the coal block, to weaken the influences of heterogeneity. For the MIP, LTNA, LF-NMR,

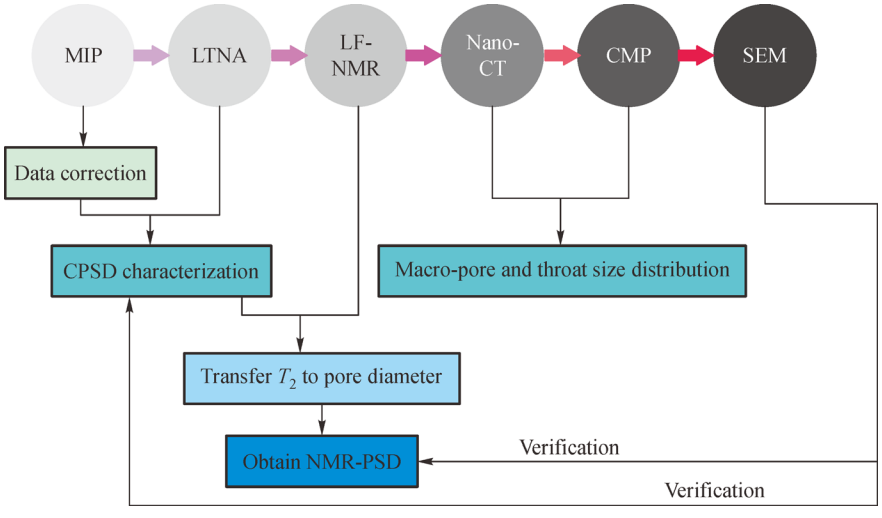

Fig. 2 Workflow diagram of this study.

Fig. 3 Pictures of all the experimental facilities: (a) Autopore IV 9500 mercury injection apparatus; (b) automatic specific surface and pore analyzer Tristar II3020; (c) LF-NMR device RecCore-2500; (d) CMP device-APSE730; (e) double beam electron microscope system FEI Helio 650; and (f) NanoVoxel-3502 series X-ray three-dimensional microscope.

Table 1 Results of the proximate analysis and coal composition of the coal samples

Sampling sites	Coal seam	Macroscopic coal petrography	$R_{o,max}$/%	Proximate analysis/%			Coal composition/%		
				M_{ad}	A_d	V_{daf}	V	I	E
WD	No. B_{43}	Semi-bright coal	0.72	2.53	4.12	32.24	34.2	62.2	3.6
KG	No. B_{41}	Semi-bright coal	0.73	3.66	5.38	36.73	57.2	41.0	1.8

Notes: WD—Wudong coalmine; KG—Kuangou coalmine; $R_{o,max}$—maximum reflectance of vitrinite, %; M_{ad}—moisture content at the air-dried basis, %; A_d—ash content at the dried basis, %; V_{daf}—volatile matter yield at the dry and ash-free basis, %; V—vitrinite content, %; I—inertinite content, %; E—exinite content, %.

CMP, and SEM tests, two samples (collected from the WD and KG, respectively) were used in each test. For the Nano-CT test, one sample (collected from the WD) was used.

3.2 MIP and LTNA

An Autopore IV 9500 mercury injection apparatus (Fig. 3(a)) was used to conduct the MIP tests using the S-I samples. The parameters of MIP test were set, including maximum mercury injection pressure of 100 MPa (corresponding to pore diameter of 18 nm), mercury surface tension of 485 dyne/cm, and contact angle of 130° (Table 2). The MIP tests in this work include evacuating the atmospheric gases and water of the sample, low-pressure mercury injection, and high-pressure mercury injection. The details on the MIP procedures can be found in international standard ISO15901-1-2005. In the MIP measurements, with the increase in the mercury intrusion pressure, significant compression in the coal matrix can be observed (Shao et al., 2018), leading to errors in the PSD measurement. Hence, the MIP data need to be corrected. An effective MIP data correction method proposed and applied by Han et al. (2015), Shao et al. (2018), and Zhang et al. (2019) was applied in this study, the details can be found in Appendix A.

An automatic specific surface and pore analyzer, Tristar II3020 (Fig. 3(b)), was applied for the LTNA tests. After high temperature drying and degassing processes, S-II were applied for LTNA tests at 77.3 K with relative pressures ranging from 0.001 to 0.995 (Table 2). The Barrett-Joyner-Halenda model, describing the capillary condensation phenomenon in cylindrical pores (Pan et al., 2017), was applied to obtain the PSD of pores with diameters between 2 nm and 50 nm based on the LTNA data. The basis of this method is to measure the quantity of nitrogen adsorbed in pores at 77.3 K as a function of its relative pressure. The details on the LTNA principles and procedures can be found in international standard ISO15901-2-2006.

3.3 LF-NMR and NMR-PSD

The fluid content and PSD can be reflected by proton nuclear magnetic resonance under radio-frequency field, and there is a consistent one-to-one match between the relaxation time (T_2) value and the pore diameter value, namely the greater T_2 is, the greater corresponding pore diameter (Li et al., 2019). In this study, a LF-NMR device named RecCore-2500 (Fig. 3(c)) developed by the Research Institute of Petroleum Exploration & Development of China was applied to detect the PSD of the S-III samples. The echo time (T_E), waiting time (T_w) and echo numbers for the LF-NMR tests, were set to 0.2 ms, 3000 ms, and 4096, respectively. Prior to the experiment, the S-III samples were first dried at 70°C for 24 h and then vacuumed for 24 h; second they were saturated in 100% distilled water for 24 h. After the experimental preparation was finished, the NMR measurements were performed at the 100% water-saturated condition for the S-III samples. More details on each LF-NMR procedure using RecCore-2500 can be found in Yao et al. (2010a, 2010b).

The relationship between the T_2 value and pore diameter was quantitatively determined by means of comparing the CPSD, derived by combining the corrected MIP data and LTNA data, and T_2 spectrum curve. In the CPSD, the PSD of the pores with diameters greater than 18 nm was characterized using corrected the MIP data, and the PSD of the pores with diameters ranging between 2 nm and 18 nm was characterized using the LTNA data. After determining the relationship between T_2 and the pore diameter, which can be referred to Appendix B, NMR-PSD can be derived after transferring T_2 to the pore diameter.

3.4 CMP

CMP can realize extremely low speed mercury intrusion. The quasi-static process of CMP cannot only distinguish the pores and throats, but also calculate pore-throat quantity ratio (Yuan and Swanson, 1989; Toledo et al., 1994). A CMP device named APSE730 (Fig. 3(d)) was used for the measurements of S-IV. The S-IV samples were first dried for 24 h at 120°C, and then mercury was injected into the samples at an extremely low speed of 0.00005 mL/min, with the pressure periodically rising and falling during the injection. The maximum injection pressure was 6.2057 MPa. Real-time monitoring and automated data acquisition, processing and output were enabled with the help of the specialized computer system. The contact angle

Table 2 Specific experimental condition of each test

Test	Specific experimental condition
MIP	The maximum mercury injection pressure, mercury surface tension, contact angle, and experimental temperature were 100 MPa, 485 dyne/cm, 130°, and 25°C, respectively
LTNA	The experimental temperature was 77.3 K with relative pressures ranging from 0.001 to 0.995
LF-NMR	The experimental temperature, resonance frequency, echo time, waiting time, and echo numbers were set to 25°C, 2.38 MHz, 0.2 ms, 3000 ms, and 4096, respectively
CMP	The mercury injection speed, maximum injection pressure, mercury surface tension, contact angle, and experimental temperature were set to 0.00005 mL/min, 6.2057 MPa, 485 dyne/cm, 130°, and 25°C, respectively
SEM	The experimental temperature, acceleration voltage, and working distance were set as 25°C, 5 kV and 4 mm, respectively
Nano-CT	The experimental temperature, X-ray source voltage and currency, and rotation step were set to 25°C, 80 kV, 95 μA, and 0.4°, respectively

and surface tension between coal and mercury were 130° and 485 dyne/cm (Table 2), respectively. The uniformity coefficient of throat (a), throat sorting coefficient (RC_{th}), and averaged pore throat ratio ($R_{av\text{-}pt}$), which are parameters reflecting the pore-throat structural complexities, can be calculated according to the following equations:

$$a = (\sum r_i a_i)/r_{max}, \quad (1)$$

$$RC_{th} = \frac{\sqrt{\sum (r_i - R_{av-th})^2 a_i}}{R_{av-th}}, \quad (2)$$

$$R_{av-pt} = \sum R_i b_i, \quad (3)$$

where, a_i is distribution frequency of normalized radius of a throat; r_i is diameter of a throat, nm; $R_{av\text{-}th}$ is averaged throat diameter value, nm; r_{max} is diameter of the largest throat, nm; R_i is pore throat ratio; b_i is distribution frequency of normalized pore-throat ratio. The greater a is, the diameters of throats of the sample are closer to those of the largest throats of the same sample, and the throat diameter of the sample is more evenly distributed. The smaller the value of RC_{th}, the closer the diameters of throats of the sample are to the mean, and the better the sorting of throats of the same sample is. The greater $R_{av\text{-}pt}$ is, the more complicated the pore-throat structure of the sample.

3.5 SEM and Nano-CT

The surfaces vertical to the bedding layer of the dry S-V samples were first polished using abrasive paper for SEM observations. Then, argon ion polishing of these surfaces was conducted using a HITACHI IM4000 argon polishing device. After drying in an oven at 65°C for 12 h and being coated with carbon to prevent electrostatic charging, the SEM maps of the S-V samples were observed using a double beam electron microscope system named FEI Helio 650 (Fig. 3(e)), with an acceleration voltage of 5 kV and a working distance of 4 mm (Table 2).

A NanoVoxel-3502 series X-ray three-dimensional microscope (Fig. 3(f)), developed by Sanying Instrument Co., Ltd., Tianjin, China, was used to detect the pore structure of the WD S-VI sample. The WD S-VI sample was scanned with an X-ray of 80 kV source voltage and a current of 95 μA. The volume data were obtained during a rotation of 360° with each rotation step equal to 0.4°. (Table 2). When the X-ray penetrated a sample, the detector received the X-ray passing through the sample, then the device converted it into a digital signal through an analog/digital converter, and finally, a three-dimensional reconstructed image data volume was obtained. To avoid the influence of moisture in the air on CT scanning, the sample was first sealed in paraffin and then scanned. The image data volume was clipped, denoised, segmented and reconstructed using Avizo 9.0 software. The pores and throats of the volume data were extracted using the local thresholding method and the 3D pore and throat structures were subsequently re-constructed. The nano-CT resolution of S-VI sample was 0.63 μm. The Pore-Network-Model (PNM) model (Dong and Blunt, 2009; Li et al., 2017b; Zhou et al., 2017a) was applied to analyze the pore and throat size distributions.

4 Results

4.1 MIP, LTNA, and LF-NMR results

The uncorrected MIP curves in Fig. 4 show that the PSDs of the two experimental HVBC samples were dominated by transition pores, followed by meso-pores, and macro-

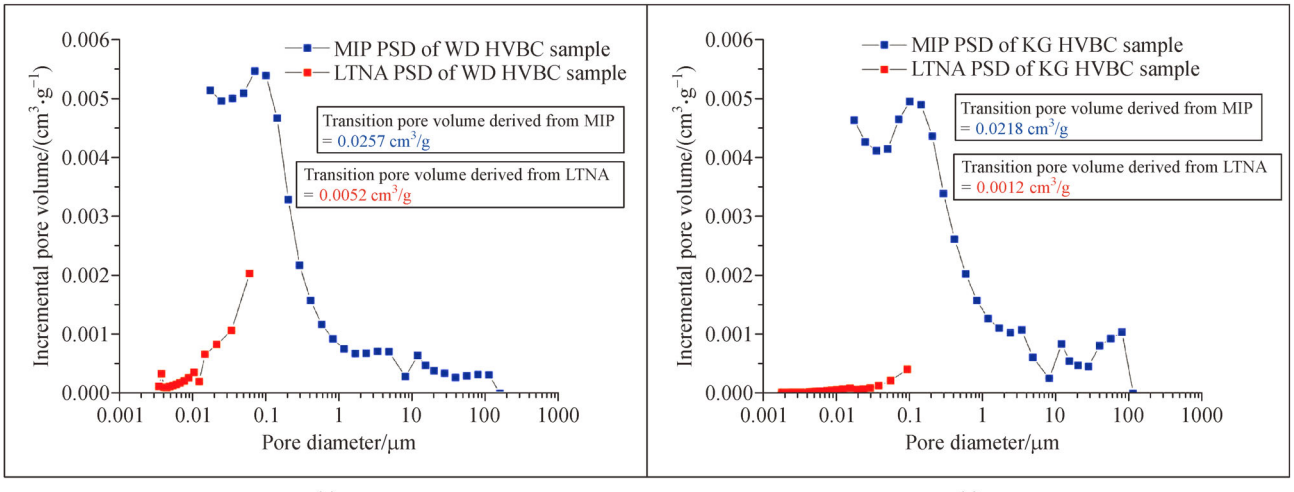

Fig. 4 PSDs of the WD sample (a) and KG sample (b) derived from MIP and LTNA.

pores, according to pore classification of Ходот (1966). The PSD of the WD sample derived from MIP (Fig. 4(a)) was very similar to that of the KG sample (Fig. 4(b)). The volumes of transition pores and meso-pores as well as macro-pores of the WD sample, derived from MIP, were 0.0257 cm^3/g, 0.0187 cm^3/g, and 0.0074 g/cm^3, respectively. The volumes of the KG sample were 0.0218 cm^3/g, 0.0229 cm^3/g, and 0.0114 cm^3/g.

The LTNA curves in Fig. 4 show that for the two HVBC samples, the transition pore volumes were greater than the micro-pore volumes. The PSD of the WD sample derived from LTNA was quite different from that of the KG sample (Fig. 4). Both the micro-pore volume (0.0017 cm^3/g) and transition pore volume (0.0052 cm^3/g) of the WD sample derived from LTNA were far greater than those of the KG sample (0.0005 cm^3/g for the micro-pore volume and 0.0012 cm^3/g for the transition pore volume). For both of the WD and KG samples, the MIP transition pore volumes were far greater than those of the LTNA transition pore volumes (Fig. 4). Explanations on this phenomenon are discussed in Section 5.1. Figure 5 demonstrates that the T_2 spectra of the two HVBC samples were bimodally distributed, manifesting as two peaks. The signal intensity of the right peak of the WD sample was greater than that of the KG sample, and the signal intensity of the left peak of the WD sample was lower than that of the KG sample. This phenomenon indicated that the volume proportion of the relatively larger pores (primarily meso-pores and macro-pores) of WD sample was greater than that of the KG sample, while the volume proportion of the relatively smaller pores (primarily micro-pores and transition pores) of the WD sample was lower than that of the KG sample.

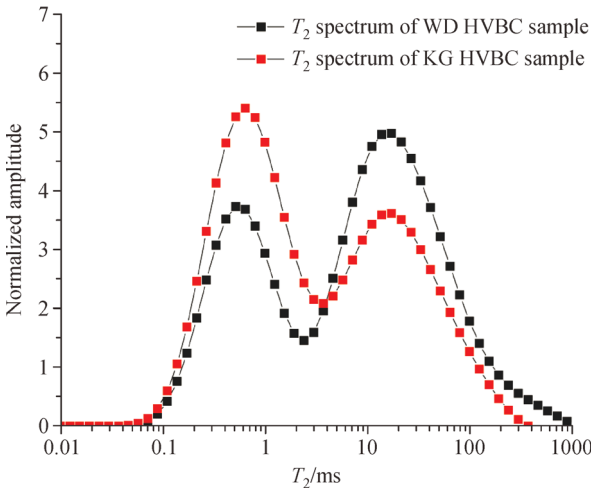

Fig. 5 T_2 spectra of the WD and KG samples.

4.2 CMP results

The diameter distributions of the macro-pores and throats of the WD and KG samples are displayed in Fig. 6. The macro-pore size distributions of the two HVBC samples were almost the same, displaying approximate peak centers. However, the throat size distribution curve of the WD sample was very different from that of the KG sample, manifesting as the narrow throat (with diameter < 20 μm) and wide throat (with diameter > 50 μm) quantities of the WD sample being greater than those of the KG sample. In particular, the range of the throat diameter of the WD sample (10–200 μm) was relatively larger than that of the KG sample (6–48 μm). Additionally, for the WD sample, more throats could contribute to the permeability (Fig. 7(a)) and the pore-throat diameter ratio distribution was wide than that of the KG sample (Fig. 7(b)). Correspondingly, the values of k_r and RC_{th} of the WD sample were greater than those of the KG sample, while values of a and $R_{av\text{-}pt}$ of the WD sample were lower than

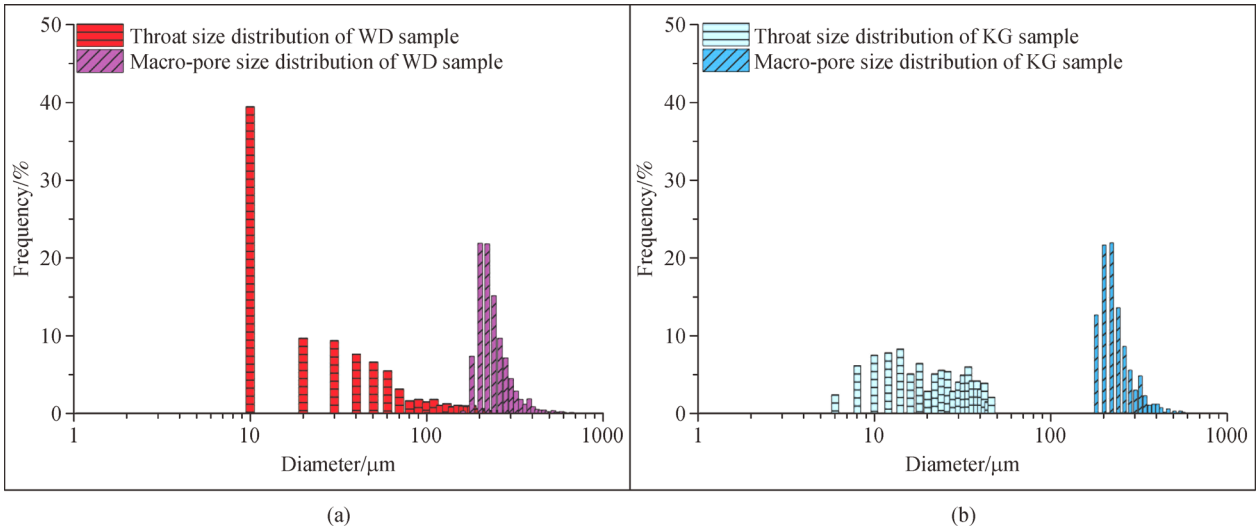

Fig. 6 Pore and throat size distributions of the (a) WD sample and (b) KG sample, derived from the CMP data.

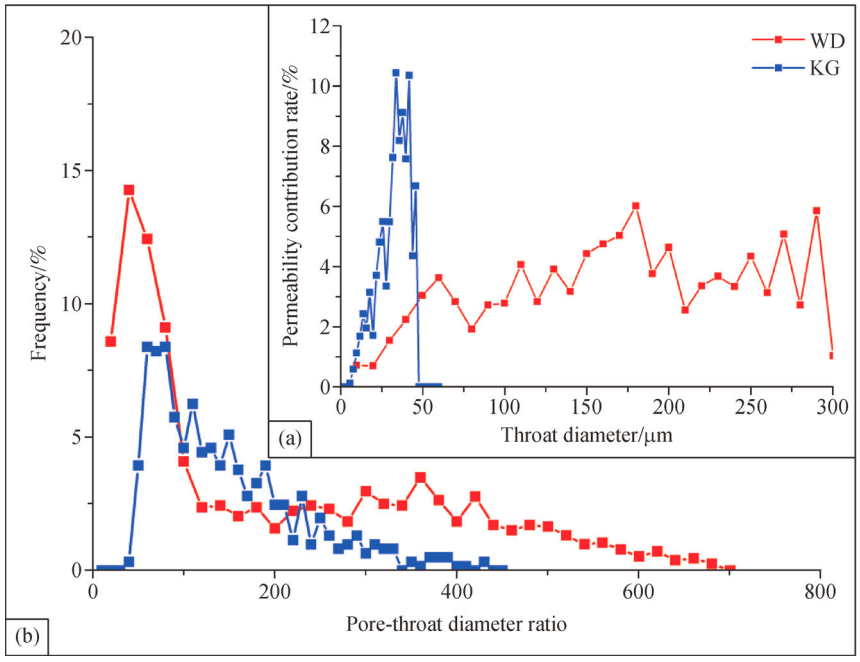

Fig. 7 Pore-throat diameter ratios and permeability contributions of the throats of the (a) WD sample (b) and KG sample.

Table 3 Parameter information of the S-IV samples applied for CMP experiment

Sample	φ_{He}/%	k_r/mD	a	RC_{th}	$R_{av\text{-}pt}$
WD S-IV	12.75	2.895	0.16	0.84	144.08
KG S-IV	10.86	0.140	0.51	0.45	201.04

Note: φ_{He}—helium porosity; k_r—Klinkenberg permeability; a—uniformity coefficient of throat; RC_{th}—throat sorting coefficient; and $R_{av\text{-}pt}$—averaged pore throat ratio.

those of the KG sample (Table 3), showing that the penetration ability of the WD sample was better than that of the KG sample.

4.3 SEM and nano-CT results

Figures 8(a)–8(c) and Figs. 8 (d)–8(f) depict the pore sizes of WD and KG S-V samples, respectively. It could be observed that pores with diameters ranging between dozens of nanometers and several microns were distributed in the two HVBC samples (Fig. 8); namely, a large number of transition pores and meso-pores as well as macro-pores were developed in the HVBC samples. Micro-pores were not easily found in the SEM map and may not have been very developed in the two HVBC samples.

Figure 9(a) shows the 2D micro-CT slice of the WD S-VI sample with a resolution of 0.63 μm. Figure 9(b) displays the details of the macro-pores of the slice in Fig. 9(a). The macro-pores with diameter greater than 1 μm were quite developed. A micro-fracture with an aperture of 3.64 μm and a macro-pore with a diameter of 19.74 μm were found. Figure 9(c) demonstrates the 3D picture of the WD S-VI sample with the color rendered. Figure 9(d) demonstrates the 3D reconstructed map of the connected macro-pores of the sub-extracted data volume. The sub-extracted data volume had dimensions of 504 μm × 504 μm × 126 μm, which was as large as possible to reflect the actual pore distribution of the WD S-VI sample. Figure 9(e) displays the pore network of Fig. 9(d), showing that the connectivity between macro-pores was very good. Figure 9(f) shows the 3D distribution of the connected and unconnected macro-pores of the sub-extracted data volume. The porosities of the former and the latter were 1.23% and 2.98%, respectively. Figure 9(g) shows the unconnected pores of the sub-extracted data volume which were marked by different colors. Figure 9(h) depicts the frequency distribution of the connected pores and throats, demonstrating that the throats with diameters ranging between 4 μm and 30 μm accounted for a dominated proportion of the total connected throat volume and that macro-pores with diameters ranging between 30 μm and 80 μm accounted for a dominated proportion of the total connected macro-pore volume.

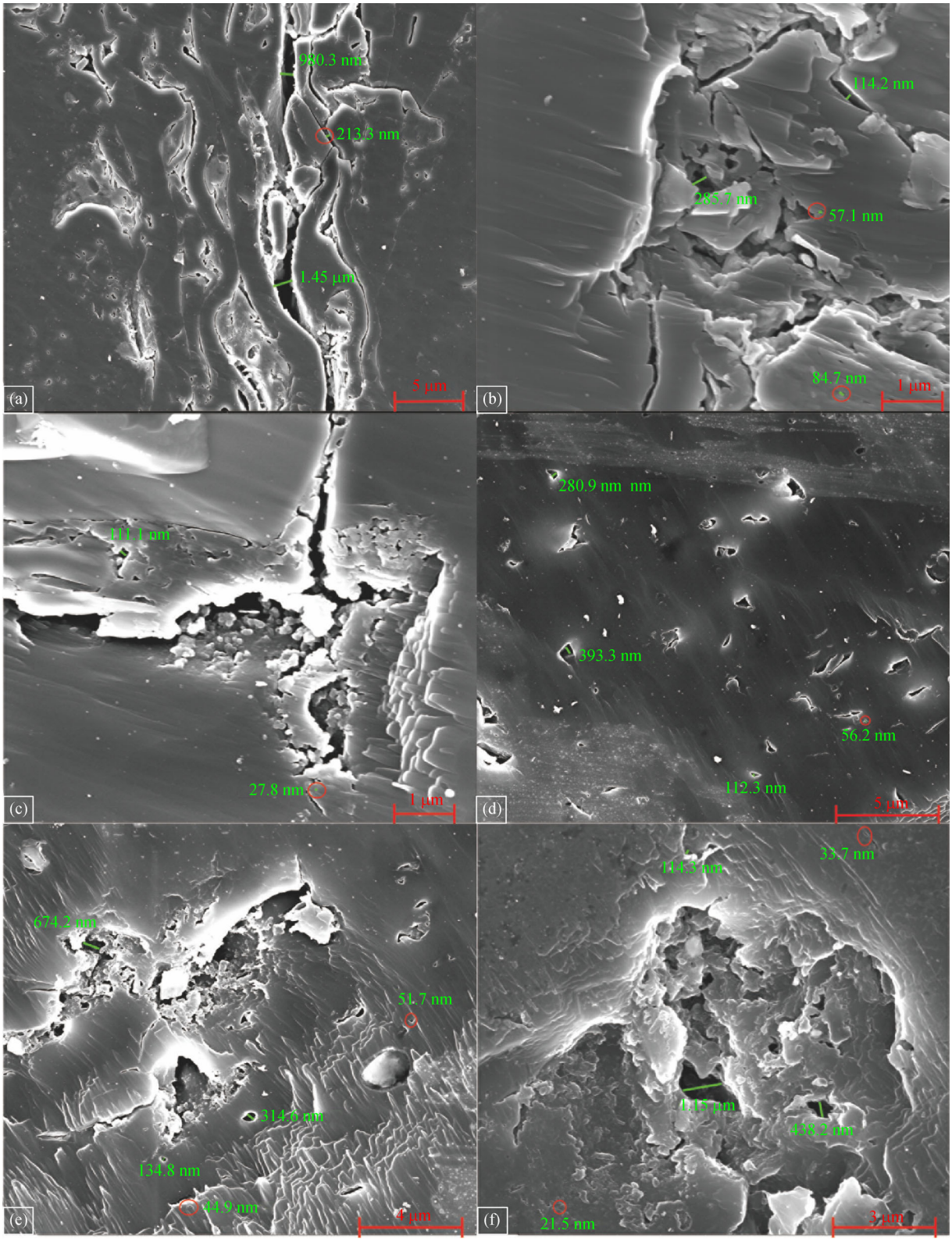

Fig. 8 SEM map of the WD sample (a–c) and KG sample (d–f).

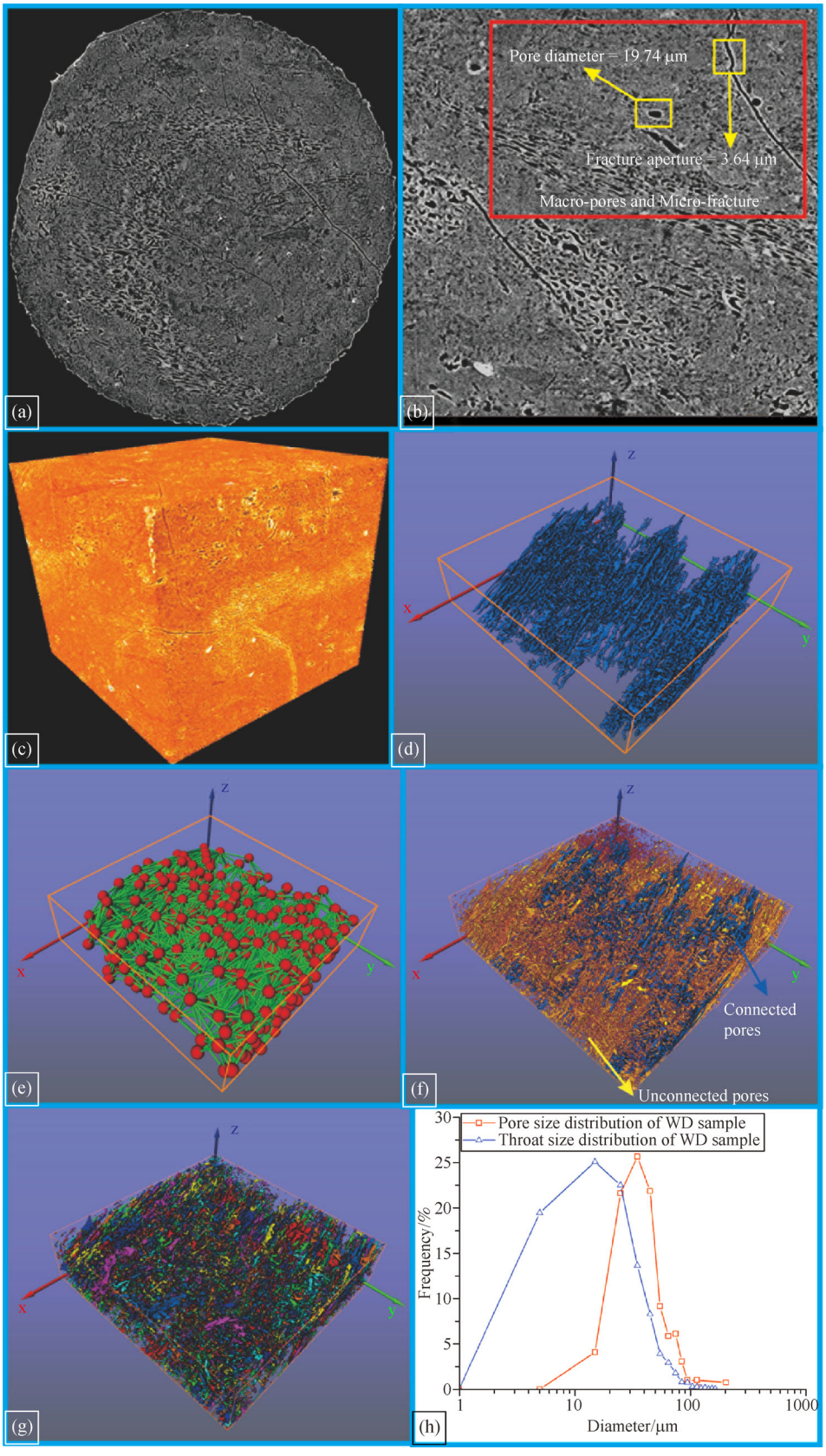

Fig. 9 Micro-CT scanning results of sample WD S-VI: (a) 2D CT slice; (b) detailed description of the 2D slice; (c) 3D structure demonstration; (d) 3D structure of the connected macro-pores; (e) 3D pore-throat skeletal structure; (f) 3D structure demonstration of the connected and unconnected macro-pores; (g) 3D distribution of the isolated macro-pores marked by different colors; and (h) macro-pore and throat size distributions.

5 Discussion

5.1 CPSD characterization

Figure 4 and Section 4.1 demonstrate that the LTNA incremental pore volumes were dramatically lower than those of the MIP data, for both HVBC samples. This phenomenon verified the conclusion that the experimental MIP data were greater than the actual situation due to coal matrix compression under high pressure mercury intrusion. Hence, the correction of the MIP data are necessary. Figure 10 demonstrates the corrected and uncorrected cumulative mercury intrusion volumes of the two HVBC samples, displaying that cumulative intrusion volume data decreased obviously after correction, particularly for the high pressure section of the cumulative curve. The decrease was insignificant at a low injection pressure, while it could be dramatic by a decrease approximately ranging between 10% and 30%, as the mercury injection pressure increased from 17.3 MPa to 100 MPa (Fig. 10). The matrix compressing coefficients of the WD and KG samples were 1.74×10^{-4} MPa^{-1} and 1.77×10^{-4} MPa^{-1}, respectively. These results were close to the compressing coefficient values of HVBC calculated by Guo et al. (2014) (1.64×10^{-4}–2.90×10^{-4} MPa^{-1} for HVBC with $R_{o,max}$ = 0.65%–0.88%) and Shao et al. (2018) (1.72×10^{-4} MPa^{-1} for HVBC with $R_{o,max}$ = 0.65%), which validated the accuracy of the correction approach of the MIP data used in this paper.

The matrix compression was negligible when mercury was injected into the pores with diameters greater than 0.1 μm, as displayed in Fig. 11. Correspondingly, the corrections of the incremental pore volumes of the two HVBC samples were slight. As mercury was injected into the transition pores with diameters ranging between 0.01 μm and 0.18 μm, the compression of the matrix was significant, and the correction of the incremental pore volume was apparent (Fig. 11). These phenomena indicated that matrix compression may mainly occur in the micro-pores and transition pores during the mercury intrusion process. The corrected incremental transition pore volume derived from the MIP was close to that derived from the LTNA data, as displayed in Fig. 12 demonstrating the CPSDs of the two HVBC samples. Hence, the CPSD approach could be regarded as a correct PSD characterization method, which took the matrix compressing issue of the MIP data and the application of the LTNA data into consideration. The CPSD of the WD sample and that of the KG sample was close, manifesting as the meso-pore volume being the greatest, followed by the transition pore volume or macro-pore volume, and the micro-pore volume was the lowest (Fig. 12). The CPSD results above were consistent with the SEM results, which showed that the transition pores and meso-pores as well as macro-pores were developed, while the micro-pores were not easily found (Fig. 7).

5.2 Full-scale PSD comparisons between the CPSD and NMR-PSD

While scholars have performed much research work on the relationship between the T_2 value and pore diameter using uncorrected MIP data (Li et al., 2015; Huang et al., 2018; Gong and Liu, 2020) or LTNA data (Tang et al., 2016) or the T_2 cutoff method (Yao et al., 2010b), they seldom work on the relationship using the CPSD data, which combines the corrected MIP data and LTNA data together and can be regarded as an approximate full-scale PSD. Considering that LF-NMR is an efficient tool for nondestructively quantifying the full-scale coal PSD (Yao and Liu, 2012), the determination of the relationship between the T_2 value and pore diameter using the CPSD data can be more accurate compared with the traditional methods using only the uncorrected MIP data or LTNA data.

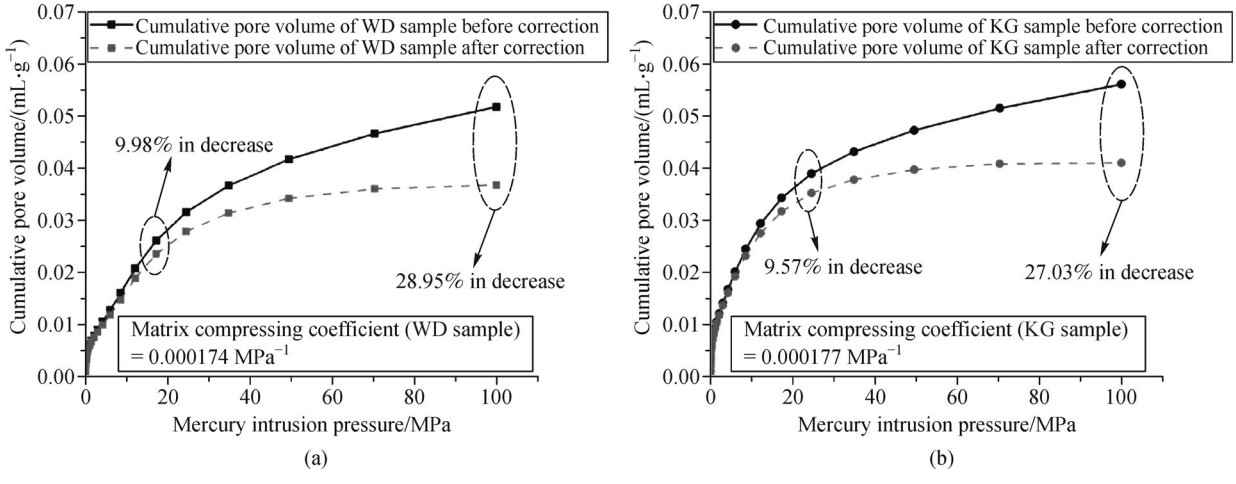

Fig. 10 Corrected and uncorrected cumulative pore volume curves derived from the MIP data: (a) WD sample; (b) KG sample.

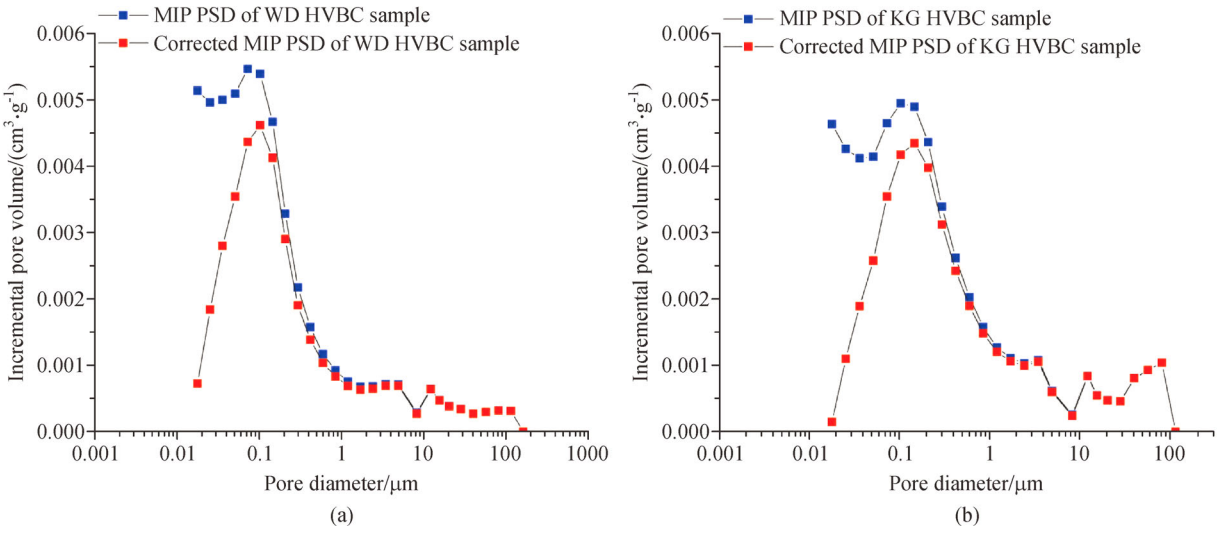

Fig. 11 Corrected and uncorrected PSDs derived from the MIP data: (a) WD sample; (b) KG sample.

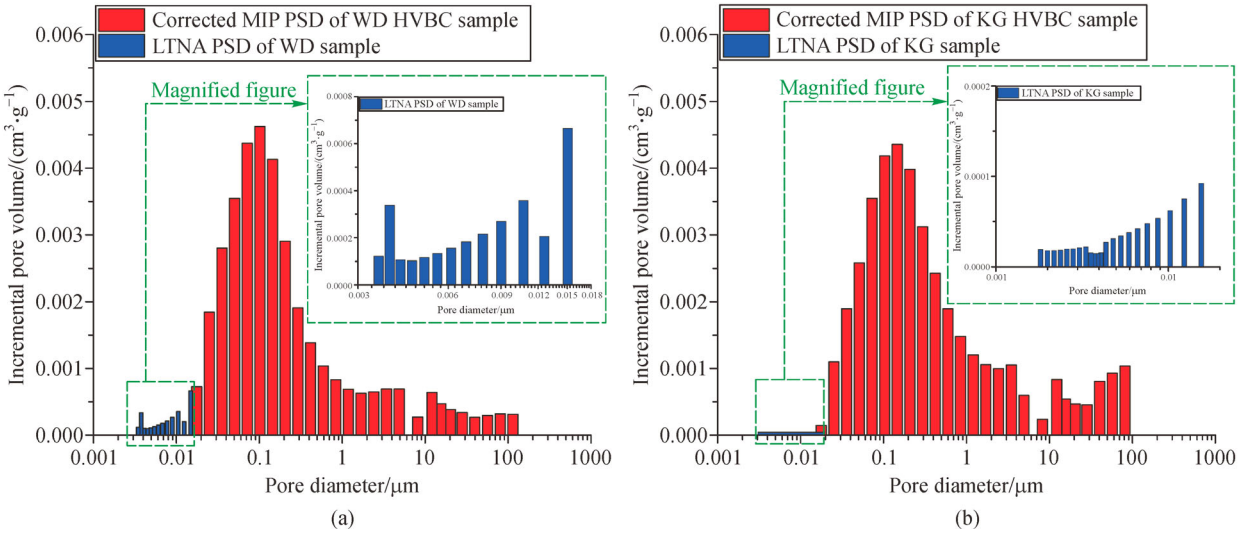

Fig. 12 CPSDs derived from the MIP and LTNA data: (a) WD sample; (b) KG sample.

By applying the determination approach described in Appendix B and using the CPSD data discussed in section 5.1, the quantitative relationships between the T_2 value and pore diameter of the two HVBC samples were revealed, as demonstrated in Fig. 13. The cumulative pore volume frequency curve derived from the CPSD was close to that derived from LF-NMR for both HVBC samples (Fig. 13). The key parameters of Eq. (B-4) were determined by applying the least-square method of Eq. (B-6). The n values of the two HVBC samples were very close while the C value of the KG sample was almost two times that of the WD sample (Fig. 13), indicating that the relationship between T_2 and the pore diameter varied for different samples, even for samples with close maceral compositions and $R_{o,max}$ values (Table 1).

The NMR-PSDs of the two HVBC samples were derived from the LF-NMR data after transferring T_2 to the pore diameter, and the comparison between the CPSD and NMR-PSD is demonstrated in Fig. 14. It can be observed that the NMR-PSDs of the two HVBC samples were overall similar to the CPSDs of the samples (Fig. 14); hence, the transfer of T_2 to the pore diameter was accurate. The macro-pore volumes derived from the NMR-PSDs were relatively lower than those derived from the CPSDs (Fig. 14). For the WD sample, the macro-pore volume derived from the CPSD was 0.0074 cm^3/g, which could be verified by the connected macro-pore volume of 0.0103 cm^3/g derived from the nano-CT of the WD S-VI sample. Hence, the characterization of the macro-pore volume derived from NMR-PSD may not be sufficiently

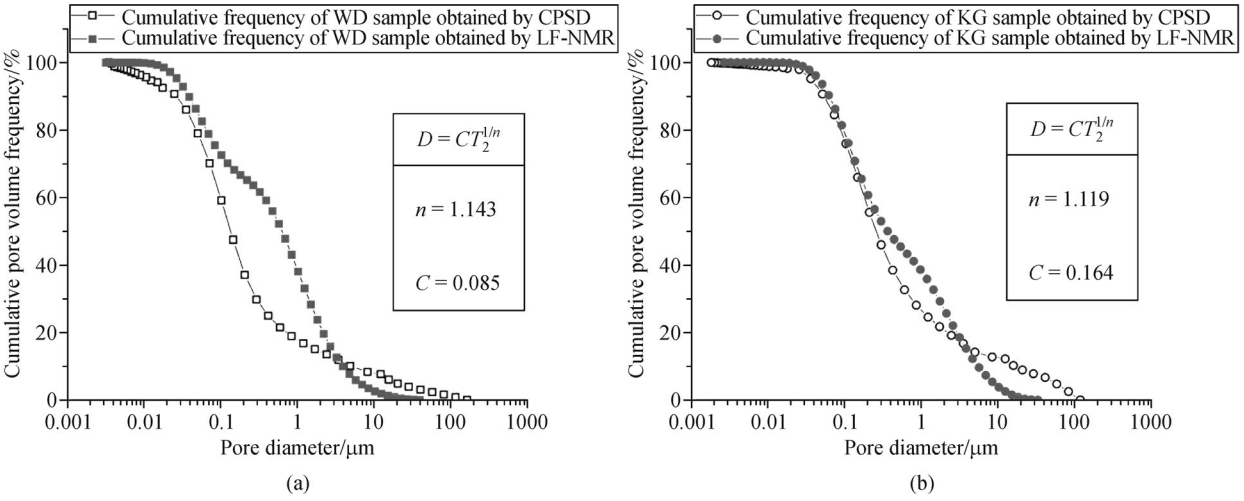

Fig. 13 Cumulative pore volume frequencies derived from the CPSD data and LF-NMR data: (a) WD sample; (b) KG sample.

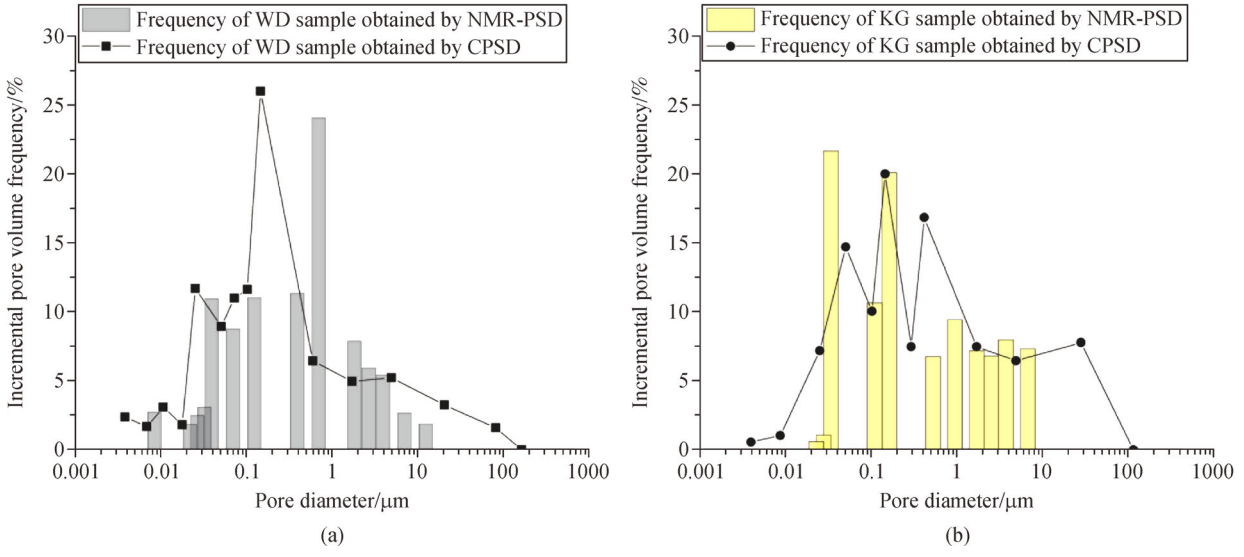

Fig. 14 PSDs derived from the LF-NMR data after transferring T_2 to the pore diameter and the PSDs derived from the CPSD data: (a) WD sample; (b) KG sample.

accurate. This phenomenon could be explained by the following reasons: 1) free water loss occurred for the macro-pores during LF-NMR testing process, although the sample was saturated before testing, leading to a lesser detected macro-pore volume; 2) systematic errors existed during the use of the method introduced in Appendix B because the method pursue to realize that the accumulative pore volume curve of the LF-NMR can mostly resemble that of the CPSD, rather than making the former completely the same as the latter.

The applications of the NMR-PSD, which were derived from the LF-NMR data after transferring T_2 to the pore diameter using the CPSD data, can be beneficial for quantitatively determining the scales of the volume-varied pores before and after reservoir stimulation for improving gas and oil recovery or reservoir damage leading to a low yield of CBM well, considering that LF-NMR is nondestructive. For instance, regarding reservoir stimulation using low temperature liquid nitrogen as reported by Qin et al. (2017), the NMR-PSD characterizations before and after stimulation using low temperature liquid nitrogen will reveal the scales of the nitrogen-stimulated pores. Clay migration is thought to be an important mechanism for reservoir damage (Kang et al., 2014; Alhuraishawy et al., 2018; Wang et al., 2019), and the migrating pathways between different scaled pores will be revealed by applying

NMR-PSD characterizations before and after reservoir damage simulation. Hence, the NMR-PSD derived from LF-NMR data after transferring T_2 to the pore diameter can be useful in gas and oil reservoir development research in future studies.

5.3 Macro-pore and throat size distributions derived from CMP and nano-CT

As introduced in Sections 4.2 and 4.3, both CMP and nano-CT technologies can characterize the distributions of the macro-pores and throats with diameters greater than 1 μm. Figure 15(a) depicts that the throat size distribution derived from nano-CT method was close to that derived from CMP, displaying that the throats with diameters ranging between 10 μm and 40 μm were the most developed. Figure 15(b) depicts that the macro-pore size distribution derived from nano-CT was very different from that derived from CMP, showing that the former macro-pore diameter was mainly concentrated in the range between 10 μm and 100 μm while the latter macro-pore diameter was mainly concentrated in the range between 200 μm and 400 μm.

The large differences in the macro-pore size distributions displayed in Fig. 15(b) can be attributed to the following reasons: 1) the S-VI sample used for the nano-CT test was approximately 1 mm in length and 1 mm in diameter to realize nanometer resolution; hence, detecting macro-pores with diameters greater than 100 μm (one tenth of the sample diameter) using nano-CT would be highly impracticable. However, the S-IV sample used for the CMP tests was 10 mm in height and 25 mm in diameter, and mercury could invade the macro-fractures with apertures greater than 100 μm or the macro-pores with diameters greater than 100 μm. In summary, the differences in the detected pore diameter ranges between the nano-CT and CMP methods led to the different results; 2) due to the first reason discussed above, the macro-pores detected by nano-CT (Fig. 15(b)) could probably be regarded as throats in the CMP tests, leading to macro-pores with diameters less than 100 μm being scarcely measured; and 3) the heterogeneities between S-IV and S-VI and the inversion process of the nano-CT volume data could influence the results as well.

5.4 Full-scale PSD of HVBC of SJR

As introduced in Section 5.1, the PSD characterization results of the WD and KG HVBC samples of this study, showed that meso-pore volume was the greatest, followed by the transition pore volume or macro-pore volume, and the micro-pore volume was the lowest. Jia et al. (2015), Luo et al. (2016), Li et al. (2017a), Tao et al. (2018), Zhang (2019), Lin et al. (2019), and Hou et al. (2020) derived the PSD of HVBC of SJR using uncorrected MIP data, and found that the micro-pore volume or transition pore volume was the greatest, and the meso-pore volume or macro-pore volume was the lowest. However, micro-pore and transition pore volumes of the same samples derived from the LTNA data in Tao et al. (2018), Lin et al. (2019), and Hou et al. (2020) were also far lower than those derived from the uncorrected MIP results. Hence, using uncorrected MIP data alone cannot accurately describe full-scale PSD because it can result in enlarged micro-pore or transition pore volumes. We reconstructed the PSD of HVBC by combining the LTNA data (2–50 nm) and uncorrected MIP data ($>$ 50 nm) of Tao et al. (2018), Lin et al. (2019), and Hou et al. (2020), and found that their

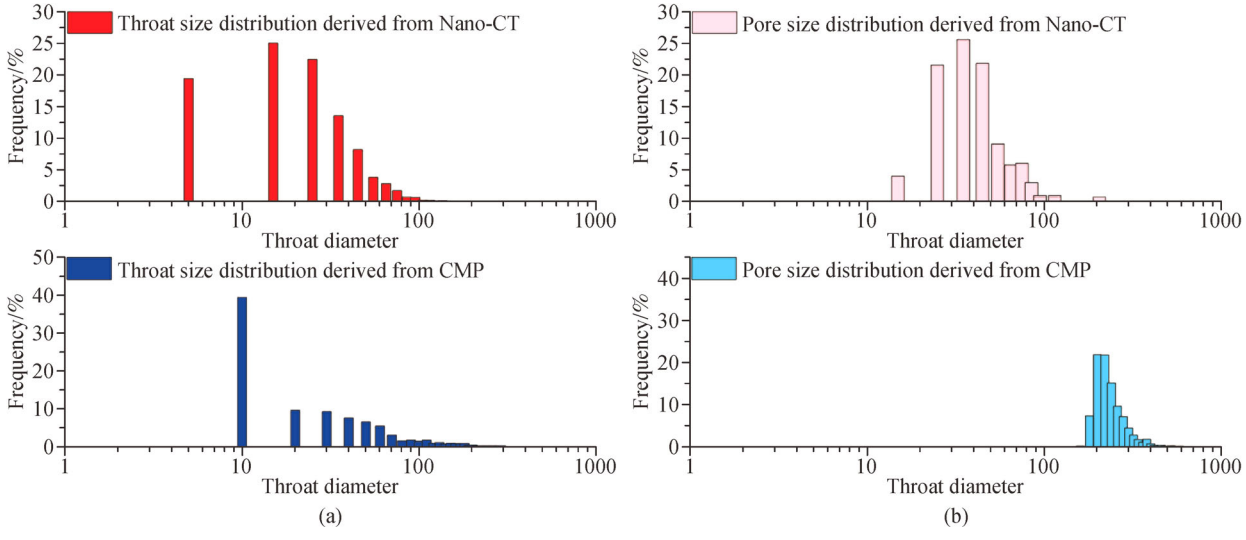

Fig. 15 (a) Throat size distributions of the WD sample derived by nano-CT and CMP metnods; (b) pore size distributions of the WD sample derived by nano-CT and CMP metnods.

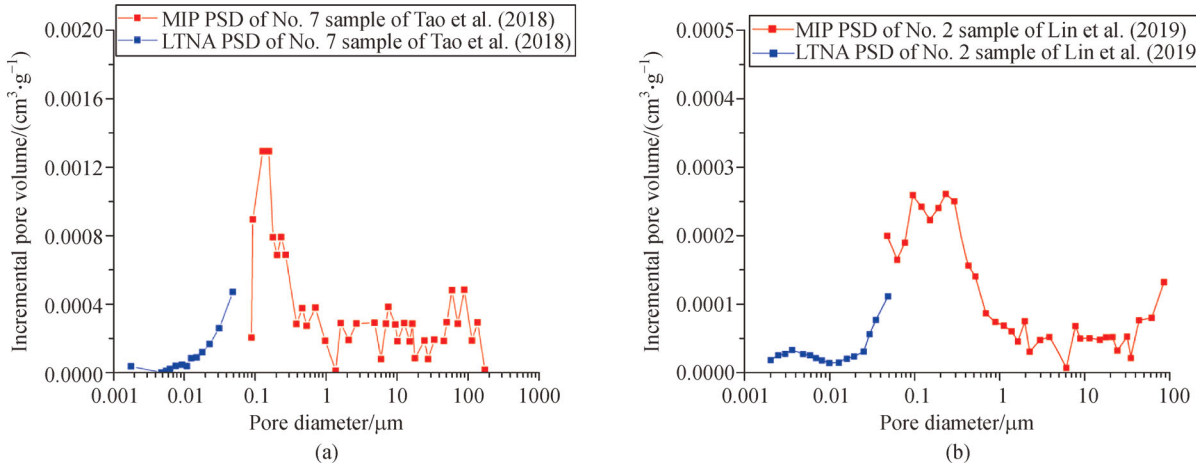

Fig. 16 Typical PSDs of HVBC derived by combining the LTNA data and uncorrected MIP data published in the work by (a) Tao et al. (2018) and (b) Lin et al. (2019).

PSD results were close to those of our study, demonstrating that for HVBC of SJB, the meso-pore volume was the greatest, followed by the transition pore volume or macro-pore volume, and the micro-pore volume was the lowest (Fig. 16). Wang et al. (2017) applied corrected MIP data and LTNA data to characterize the PSD of HVBC with different macrolithotypes. We reconstructed the PSD of HVBC by combining the LTNA data (2–50 nm) and corrected MIP data (> 50 nm) of Wang et al. (2017), and found that the overall meso-pore volume was the greatest, followed by the macro-pore volume, and the transition pore volume or micro-pore volume was the lowest (Fig. 17). This result was also close to that of our study, and all the data discussed in this section validated that full-scale PSD characterization using the LTNA data and corrected MIP data are relatively more accurate than that derived from the uncorrected MIP data alone.

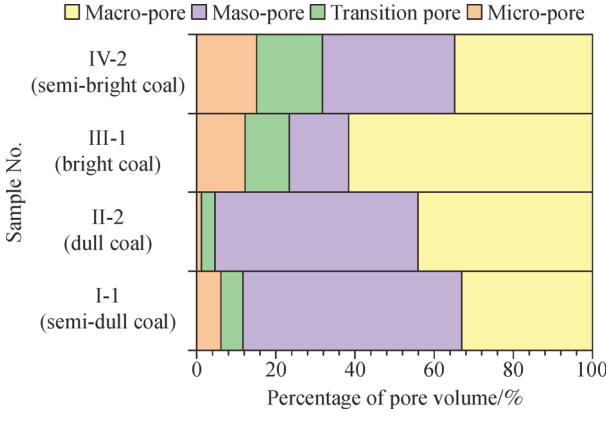

Fig. 17 PSDs of HVBC derived by combining the LTNA data and corrected MIP data published in Wang et al. (2017).

6 Conclusions

The main conclusions are summarized as follows:

1) The CPSD, combining the corrected MIP data and LTNA data, can be regarded as a correct method for the PSD characterization of HVBC in this study;

2) For HVBC of SJB, meso-pore volume was the greatest, followed by transition pore volume or macro-pore volume, and micro-pore volume was the lowest;

3) LF-NMR can accurately characterize PSD after transferring T_2 to the pore diameter using the CPSD data;

4) The relationship between T_2 and the pore diameter varied for different samples, even for samples with close macerals compositions and $R_{o,max}$ values;

5) The throat size distribution derived from nano-CT method was close to that derived from CMP; however, because of the differences in the detected pore diameter ranges of the nano-CT and CMP methods, the macro-pore size distribution derived from nano-CT was very different from that derived from CMP.

Acknowledgements This work was supported by the Opening Fund of Key Laboratory of Continental Shale Accumulation and Development (North-east Petroleum University), Ministry of Education; the National Science and Technology Major Project of the Ministry of Science and Technology of China (No. 2016ZX05043-004-001); and the National Natural Science Foundation of China (Grant No. 41772158).

Appendix A

The coal matrix compressibility can be expressed as:

$$K_c = -\frac{dV_c}{V_c dP}, \quad \text{(A-1)}$$

where, K_c is the coal matrix compressibility, MPa^{-1}; V_c is the coal matrix volume, cm^3/g; and dV_c/dP is the change in

the coal matrix volume as mercury injection pressure changes, $cm^3/(g \cdot MPa)$.

For compressible porous coal, the following equation exists during mercury injection:

$$\Delta V_o = \Delta V_p + \Delta V_c, \tag{A-2}$$

where, ΔV_o, ΔV_p and ΔV_c are the injected pore volume, filling pore volume, and compressing matrix volume, respectively, g/cm^3.

A proportional relationship between ΔV_o and P was found for the HVBC samples in this study as P increased from 35 MPa (corresponding to pores with 51.0 nm in diameter) to 100 MPa (corresponding to pores with a diameter of 18 nm) (Fig. 9), and the proportional constant β can be expressed as:

$$\beta = \frac{\Delta V_o}{\Delta P}. \tag{A-3}$$

Combining Eqs. (A-1), (A-2) and (A-3), it can be found that:

$$K_c = \frac{1}{V_c}\left(\beta - \frac{\Delta V_{p1}}{\Delta P}\right), \tag{A-4}$$

where, ΔV_{p1} is the volume of pores with diameters ranging between 18 nm and 51.0 nm, which can be obtained from LTNA data.

Assuming that K_c is a constant during mercury injection, the coal matrix volume can be corrected using the following equation:

$$V_{c(P_i)} = V_c - \frac{\Delta V_p}{\Delta P}(P_i - P_0), \tag{A-5}$$

where, $V_{c(P_i)}$ is the coal matrix volume under the mercury injection pressure of P_i, cm^3/g; P_0 is the initial injection pressure and is equal to 0.0035 MPa.

Then the actual mercury filling pore volume can be calculated:

$$V_{P_i} = V_{o(P_i)} - K_c V_{c(P_i)}(P_i - P_0), \tag{A-6}$$

where, V_{P_i} and $V_{o(P_i)}$ are the actual mercury filling pore volume and actual injected pore volume under the pressure of P_i, respectively, cm^3/g.

Appendix B

The fluid content and pore structure can be reflected by proton nuclear magnetic resonance under radio-frequency field. The relaxation characteristics can be expressed as:

$$\frac{1}{T_2} \approx \rho_2 \frac{S}{V} = F_s \frac{\rho_2}{r}, \tag{B-1}$$

where, T_2 represents the transverse relaxation time, ms; S represents the pore surface area, μm^2; V is the pore volume, μm^3; ρ_2 denotes the transverse surface relaxivity coefficient, μm/ms; r is the pore radius, μm; and F_s represents the geometry factor. Therefore, there is a consistent one-to-one match between T_2 value and the pore radius.

Equation (B-1) can be transferred to Eq. (B-2), namely:

$$T_2 = \frac{r}{\rho_2 F_s}. \tag{B-2}$$

In the actual situation, the pores in rocks are quite complex and previous studies (Li et al., 2015; Huang et al., 2018) found the following relationship between T_2 and r:

$$T_2 = \frac{r^n}{\rho_2 F_s}, \tag{B-3}$$

where, n is a power exponent constant. Define $C = 2 \times (\rho_2 F_s)^{1/n}$ and Eq. (B-3) can be expressed as:

$$D = C T_2^{1/n}, \tag{B-4}$$

where, D is the pore diameter, μm. In this study, MIP data could reflect PSD of pores with diameters greater than 18 nm, and the increment pore volume derived from MIP was greater than the actual pore volume due to the compressibility of the coal matrix. Hence, the PSD of the pores with diameters greater than 18 nm was obtained using the corrected MIP data as illustrated in Appendix A, and the PSD of the pores with diameters ranging between 2 nm and 18 nm was derived from the LTNA data. Therefore, the comprehensive PSD (CPSD) derived from the corrected MIP data and LTNA data was addressed. The T_2 curve derived using a water saturated specimen can describe the PSD of all the pores in coal. Comparing the T_2 curve and CPSD, the unknown parameters in Eq. (B-4) can be calculated. The details are as follows:

Take logarithm on both sides of the Eq. (B-4):

$$\ln r = \ln C + \frac{1}{n}\ln T_2. \tag{B-5}$$

Based on the least-square method, the values of C and n can be derived by calculating the minimum value of L, which can be expressed as:

$$L = \sum_{i=1}^{m} \left[\frac{1}{n}\ln T_2 + \ln C - \ln r\right]^2. \tag{B-6}$$

References

Alhuraishawy A K, Bai B J, Wei M Z, Geng J M, Pu J Y (2018). Mineral dissolution and fine migration effect on oil recovery factor by low salinity water flooding in low-permeability sandstone reservoir. Fuel, 220: 898–907

Bai B, Zhu R, Wu S, Yang W, Gelb J, Gu A, Zhang X, Su L (2013). Multi-scale method of Nano (Micro)-CT study on microscopic pore structure of tight sandstone of Yanchang Formation, Ordos Basin. Pet Explor Dev, 40(3): 354–358

Bale H D, Schmidt P W (1984). Small-angle X-ray-scattering investigation of submicroscopic porosity with fractal properties. Phys Rev Lett, 53(6): 596–599

Cai Y D, Liu D M, Yao Y B, Li J Q, Liu J L (2011). Fractal characteristics of coal pores based on classic geometry and thermodynamics models. Acta Geol Sin-Engl, 85(5): 1150–1162

Cooper J R, Crelling J C, Rimmer S M, Whittington A G (2007). Coal metamorphism by igneous intrusion in the Raton Basin, CO and NM: implications for generation of volatiles. Int J Coal Geol, 71(1): 15–27

Dong H, Blunt M J (2009). Pore-network extraction from micro-computerized-tomography images. Phys Rev E Stat Nonlin Soft Matter Phys, 80(3): 1–11

Fu H J, Tang D Z, Xu H, Xu T, Chen B L, Hu P, Yin Z Y, Wu P, He G J (2016). Geological characteristics and CBM exploration potential evaluation: a case study in the middle of the southern Junggar Basin, NW China. J Nat Gas Sci Eng, 30: 557–570

Fu H J, Tang D Z, Xu T, Xu H, Tao S, Li S, Yin Z Y, Chen B L, Zhang C, Wang L L (2017). Characteristics of pore structure and fractal dimension of low-rank coal: a case study of Lower Jurassic Xishanyao coal in the southern Junggar Basin, NW China. Fuel, 193: 254–264

Gomord O F, Soete J, Davy C A, Janssens N, Troadec D, Cazaux F, Caline B, Swennen R (2017). Tight chalk: characterization of the 3D pore network by FIB-SEM, towards the understanding of fluid transport. J Petrol Sci Eng, 156: 67–74

Gong Y J, Liu K Y (2020). Pore throat size distribution and oiliness of tight sands–a case study of the southern Songliao Basin, China. J Petrol Sci Eng, 184: 106508

Guan S W, Chen Z X, Fang S H (2012). Three potential exploration areas of southern Junggar Basin, NW China: arguments from structural modeling. Pet Explor Dev, 39(1): 43–50

Guo X Q, Yao Y B, Liu D M (2014). Characteristics of coal matrix compressibility: an investigation by mercury intrusion porosimetry. Energy Fuels, 28(6): 3673–3678

Han B B, Qin Y, Zhang Z, Wang G, Yu P (2015). Study on coal compressibility and correction of compression amount based on compressibility of mercury injection test. Coal Sci Technol, 43: 68–72 (In Chinese)

Hou H H, Shao L Y, Tang Y, Zhao S, Yuan Y, Li Y A, Mu G Y, Zhou Y, Liang G D, Zhang J Q (2020). Quantitative characterization of low-rank coal reservoirs in the southern Junggar Basin, NW China: implications for pore structure evolution around the first coalification jump. Mar Pet Geol, 113: 104165

Huang H X, Sun W, Ji W M, Zhang R H, Du K, Zhang S H, Ren D Z, Wang Y W, Chen L, Zhang X (2018). Effects of pore-throat structure on gas permeability in the tight sandstone reservoirs of the Upper Triassic Yanchang Formation in the Western Ordos Basin, China. J Petrol Sci Eng, 162: 602–616

Jia B Y, Jin X L, Li J W, Wu X B, Xu J J (2015). Calculation of free gas content of low rank coal reservoirs: a case study of the southeast margin of Junggar Basin. Coal Geology and Exploration, 43(02): 33–36 + 43. (in Chinese).

Kang J Q, Fu X H, Liang S, Zhou F R, Li Y S (2018). Experimental study of changes in fractures and permeability during nitrogen injection and sealing of low-rank coal. J Nat Gas Sci Eng, 57: 21–30

Kang Y L, Xu C Y, You L J, Yu H F, Zhang B J (2014). Comprehensive evaluation of formation damage induced by working fluid loss in fractured tight gas reservoir. J Nat Gas Sci Eng, 18: 353–359

Karacan C Ö, Okandan E (2000). Fracture/cleat analysis of coals from Zonguldak Basin (northwestern Turkey) relative to the potential of coalbed methane production. Int J Coal Geol, 44(2): 109–125

Li A F, Ren X X, Wang G J, Wang Y Z, Jiang K L (2015). Characterization of pore structure of low permeability reservoirs using a nuclear magnetic resonance method. Journal of China University of Petroleum, 39(6): 92–98 (in Chinese)

Li X, Fu X H, Ranjith P G, Xu J (2019). Stress sensitivity of medium- and high volatile bituminous coal: an experimental study based on nuclear magnetic resonance and permeability porosity tests. J Petrol Sci Eng, 172: 889–910

Li X, Fu X H, Yang X S, Ge Y Y, Quan F K (2018). Coalbed methane accumulation and dissipation patterns: a case study of the Junggar Basin, NW China. J Asian Earth Sci, 160: 13–26

Li Y Y, Jiang L H, Zhang D W, Zhang Y G (2017a). Characteristics of the pore and fracture in Fukang mining area. Coal Geology and Exploration, 45(02): 80–84 (in Chinese)

Li Z T, Liu D M, Cai Y D, Ranjith P G, Yao Y B (2017b). Multi-scale quantitative characterization of 3-D pore-fracture networks in bituminous and anthracite coals using FIB-SEM tomography and X-ray μ-CT. Fuel, 209: 43–53

Lin H F, Bu J J, Yan M, Bai Y (2019). Joint analysis of pore structure characteristics of middle and low rank coal with nitrogen adsorption and mercury intrusion method. Journal of Xi'an University of Science and Technology, 39(01): 1–8 (in Chinese)

Liu S M, Zhang R, Karpyn Z, Yoon H, Dewers T (2019). Investigation of accessible pore structure evolution under pressurization and adsorption for coal and shale using small-angle neutron scattering. Energy Fuels, 33(2): 837–847

Liu X F, Nie B S (2016). Fractal characteristics of coal samples utilizing image analysis and gas adsorption. Fuel, 182: 314–322

Luo L, Tang D Z, Tao S, Xu H, Li S, Meng Y J (2016). Pore structure and its influence on gas mass transfer of low rank coal in eastern Junggar Basin, Xinjiang. Journal of China Coal Society, 41(04): 941–947 (in Chinese)

Mao J H, Xu H L (1999). Evaluation and Prediction of Chinese Coal Resources. Beijing: Science Press

Ni X M, Miao J, Lv R S, Lin X Y (2017). Quantitative 3D spatial characterization and flow simulation of coal macropores based on uCT technology. Fuel, 200: 199–207

Okolo G N, Everson R C, Neomagus H W J P, Roberts M J, Sakurovs R (2015). Comparing the porosity and surface areas of coal as measured by gas adsorption, mercury intrusion and SAXS techniques. Fuel, 141: 293–304

Pan J N, Niu Q H, Wang K, Shi X H, Li M (2016). The closed pores of tectonically deformed coal studied by small-angle X-ray scattering and liquid nitrogen adsorption. Microporous Mesoporous Mater, 224: 245–252

Pan J N, Peng C, Wan X Q, Zheng D S, Lv R S, Wang K (2017). Pore structure characterstics of coal-bearing organic shale in Yuzhou coalfield, China using low pressure N_2 adsorption and FESEM methods. J Petrol Sci Eng, 153: 234–243

Qin L, Zhai C, Liu S M, Xu J Z, Yu G Q, Sun Y (2017). Changes in the petrophysical properties of coal subjected to liquid nitrogen freeze-

thaw-A nuclear magnetic resonance investigation. Fuel, 194: 102–114

Sang G J, Liu S M, Zhang R, Elsworth D, He L L (2018). Nanopore characterization of mine roof shales by SANS, nitrogen adsorption, and mercury intrusion: impact on water adsorption/retention behavior. Int J Coal Geol, 200: 173–185

Shao P, Wang X, Song Y, Li Y (2018). Study on the characteristics of matrix compressibility and its influence factors for different rank coals. J Nat Gas Sci Eng, 56: 93–106

Shi X H, Pan J N, Hou Q L, Jin Y, Wang Z Z, Niu Q H, Li M (2018). Micrometer-scale fractures in coal related to coal rank based on micro-CT scanning and fractal theory. Fuel, 212: 162–172

Song Y, Jiang B, Li F L, Liu J G (2017). Structure and fractal characteristic of micro- and meso-pores in low, middle-rank tectonic deformed coals by CO_2 and N_2 adsorption. Microporous Mesoporous Mater, 253: 191–202

Tang H M, Gong X P, Tang H X, Zhang L H, Zhao F, He Y (2016). Evaluation method and damage mechanism of shale formation sensitivity damage. J Cent South Univ, 47(4): 1228–1236

Tao S, Chen S D, Tang D Z, Zhao X, Xu H, Li S (2018). Material composition, pore structure and adsorption capacity of low-rank coals around the first coalification jump: a case of eastern Junggar Basin, China. Fuel, 211: 804–815

Tian J J, Yang S G (2011). Sequence strata and coal accumulation of lower and middle Jurassic formation from southern margin of Junggar Basin, Sinking, China. J China Coal Soc, 36: 58–64 (in Chinese)

Toledo P G, Scriven L E, Davis H T (1994). Pore-space statistics and capillary pressure curves from volume-controlled. SPE J, 9(01): 46–54

Wang A M, Wei Y C, Yuan Y, Li C F, Li Y, Cao D Y (2017). Coalbed methane reservoirs' pore-structure characterization of different macrolithotypes in the southern Junggar Basin of northwest China. Mar Pet Geol, 86: 675–688

Wang B Y, Qin Y, Shen J, Wang G, Zhang Q S, Liu M (2019). Experimental study on water sensitivity and salt sensitivity of lignite reservoir under different Ph. J Petrol Sci Eng, 172: 1202–1214

Wang Z, Pan J, Hou Q, Yu B, Li M, Niu Q (2018). Anisotropic characteristics of low-rank coal fractures in the Fukang mining area, China. Fuel, 211: 182–193

Ходот В В (1966). Coal and Gas Outburst. Beijing: China Industry Press (in Chinese)

Yao Y B, Liu D M (2012). Comparison of low-field NMR and mercury intrusion porosimetry in characterizing pore size distributions of coals. Fuel, 95: 152–158

Yao Y B, Liu D M, Cai Y D, Li J Q (2010a). Advanced characterization of pores and fractures in coals by nuclear magnetic resonance and X-ray computed tomography. Sci China Earth Sci, 53(6): 854–862

Yao Y B, Liu D M, Che Y, Tang D Z, Tang S H, Huang W H (2010b). Petrophysical characterization of coals by low-field nuclear magnetic resonance (NMR). Fuel, 89(7): 1371–1380

Yao Y B, Liu D M, Tang D Z, Tang S H, Huang W H, Liu Z H, Che Y (2009). Fractal characterization of seepage-pores of coals from China: an investigation on coal permeability of coals. Comput Geosci-UK, 36(6): 1159–1166

Yuan H H, Swanson B F (1989). Resolving pore space characteristics by rate-controlled porosimetry. SPE Form Eval, 4(01): 17–24

Zhang J, Wei C, Ju W, Yan G, Lu G, Hou X, Kai Z (2019). Stress sensitivity characterization and heterogeneous variation of the pore-fracture system in middle-high rank coals reservoir based on NMR experiments. Fuel, 238: 331–344

Zhang M, Fu X H, Wang H D (2018). Analysis of physical properties and influencing factors of middle-rank coal reservoirs in China. J Nat Gas Sci Eng, 50: 351–363

Zhang Y Y (2019). Study on heterogeneity of coal reservoirs in Fukang Mining Area on the southern margin of Junggar Basin. Dissertation for the Master's Degree. Urumqi: Xinjiang University (in Chinese)

Zhao F H, Ren D Y (1995). The application of high-resolution transmission electron microscopy to study the structures of coal macerals. Geological Review, 41(6): 564–570 (in Chinese)

Zhao J L, Tang D Z, Qin Y, Xu H, Lv Y M, Tao S, Li S (2017). Evaluation of fracture system for coal marcolithotypes in the Hancheng Block, eastern margin of the Ordos Basin, China. J Petrol Sci Eng, 159: 799–809

Zhou S D, Liu D M, Cai Y D, Karpyn Z, Yao Y B (2018a). Comparative analysis of nanopore structure and its effect on methane adsorption capacity of southern Junggar coalfield coals by gas adsorption and FIB-SEM tomography. Microporous Mesoporous Mater, 272: 117–128

Zhou S D, Liu D M, Cai Y D, Karpyn Z, Yao Y B (2018b). Petrographic controls on pore and fissure characteristics of coals from the southern Junggar Coalfield, northwest China. Energies, 11(6): 1556

Zhou S D, Liu D M, Cai Y D, Yao Y B, Che Y, Liu Z H (2017b). Multi-scale fractal characterizations of lignite, subbituminous and high-volatile bituminous coals pores by mercury intrusion porosimetry. J Nat Gas Sci Eng, 44: 338–350

Zhou S D, Liu D M, Cai Y D, Yao Y B, Li Z T (2017a). 3D characterization and quantitative evaluation of pore-fracture networks of two Chinese coals using FIB-SEM tomography. Int J Coal Geol, 174: 41–54

Zhou S D, Liu D M, Cai Y D, Yao Y B (2016). Gas sorption and flow capabilities of lignite, subbituminous and high volatile bituminous coals in the southern Junggar Basin, NW China. J Nat Gas Sci Eng, 34: 6–21

Author Biographies

Prof. Wanchun Zhao received his Ph.D Degree (Candidate of Oil-Gas Well Engineering) in 2009 from Northeast Petroleum University, Daqing, China. He is currently a petroleum geology engineer and professor at Northeast Petroleum University.

He has published personally and in cooperation with colleagues more than 50 papers. His research focuses on oil and gas reservoir characterization, reservoir stimulation, and reservoir drilling.

Prof. Zhao is also one of the members of Society of Petroleum Engineers (SPE).

E-mail: zhaowanchun@nepu.edu.cn.

Dr. Xin Li recieved his Ph.D Degree (Candidate of Geological Resources and Geological Engineering) in 2018 from China

University of Mining and Technology, Xuzhou, China. He is currently an associate professor at Xinjiang University, China.

He has published personally and in cooperation with colleagues more than 20 papers. His research focuses on unconventional oil and gas reservoir characterization and reservoir damage.

E-mail: lixinwaxj@xju.edu.cn.

Prof. Tingting Wang recieved his Ph.D Degree (Candidate of Oil and Gas Engineering) in 2017 from Northeast Petroleum University, Daqing, China. She is currently a petroleum engineering professor at Northeast Petroleum University.

She has published personally and in cooperation with colleagues more than 20 papers. His research focuses on oil and gas reservoir development.

E-mail: wttlovework@163.com.

Prof. Xuehai Fu recieved his Ph.D Degree (Candidate of Mineral prospecting and Exploration) in 2001 from China University of Mining and Technology (Beijing), Beijing, China. He is currently a professor at China University of Mining and Engineering, Xuzhou, China.

He has published personally and in cooperation with colleagues more than 150 papers. His research focuses on unconventional oil and gas reservoir development.

E-mail: fuxuehai@cumt.edu.cn.